Data-Driven Diagnosis of Measurement Biases for Filtered Rayleigh Scattering

Evan P. Warner[1,*], Gwibo Byun[1], K. Todd Lowe[1]

1: Kevin T. Crofton Dept. of Aerospace and Ocean Engineering, Virginia Tech, Blacksburg VA, USA

*Corresponding author: evanpw3@vt.edu

Keywords: Filtered Rayleigh Scattering, Data-Driven, and Laser Rayleigh Scattering.

ABSTRACT

This work focuses on the data mining of a filtered Rayleigh scattering (FRS) database to diagnose the source(s) of measurement biases experienced in these applied measurements in harsh environments. Qualitative statistical analysis is performed to assess modeled-to-measured signal disagreements. This qualitative analysis shows that the signal model converges to measured signals as the non-dimensional thermodynamic parameter, termed the Y-parameter for Rayleigh scattering analysis, decreases. To perform a quantitative assessment, these FRS datasets were processed for Y and compared to known values for Y derived from reference measurements of the corresponding flow fields. Residuals between the FRS results and the reference values for Y were plotted as a histogram, which showed that there is a region of "least-bias" corresponding to $Y \leq 1$. Root cause assessment of bias sources suggests that the key contributing factor is uncertainty in the modeled Rayleigh-Brillouin scattering signal for air when $Y > 1$.

1. Introduction

For aerodynamic measurements in harsh environments, non-intrusive, particle-free diagnostic techniques are attractive because they can provide flow field information in areas where it is impractical to place probe instrumentation. Additionally, laser-optical techniques such as laser Rayleigh scattering (LRS), filtered Rayleigh scattering (FRS), and Raman scattering leverage how laser light scatters off of molecules naturally present in the flow field of interest, which can provide rich, multi-property information about the fluid flow.

FRS measurements conducted at Virginia Tech for applied turbomachinery measurements have shown that measured signals do not agree with modeled signals at known conditions for certain measurement configurations. This disagreement has led to large biases in flow properties of interest from FRS data. The diagnosis of this disagreement is needed in order to create a reliable measurement system over a significant range of operating conditions. This work will take a data-driven approach to diagnosing this modeled-to-measured disagreement by analyzing an extensive FRS database.

FRS is a non-intrusive, laser-based optical diagnostic technique that can be used to obtain simultaneous measurements of static temperature, static density, and 3-component velocity of aerodynamic flows (Miles et al. (1991, 1996); Forkey (1996); Boguszko & Elliott (2005); Doll et al. (2014, 2016); Cutler & Lowe (2023)). As its name suggests, FRS is a filtering of the LRS signature induced by the elastic scattering of laser light off of a collection of molecules in a particular medium of interest. For aerodynamic measurements, the medium of interest is, generally, air. In addition to LRS, scattering off of larger particulates (Mie scattering) and/or from geometry (geometric/background scattering) in the vicinity of the measurement volume can overwhelm the LRS signal of interest. The primary motivation of FRS is to filter out the undesired light scattering contributions from Mie and geometric scattering, and solely collect content from the LRS signal. The filtering mechanism for this technique is a molecular vapor filter, which filters the spectral content of the LRS, Mie, and geometric scattering signals. A visual for the spectral filtering phenomena of FRS is shown in Fig. 1 below. The type of vapor to use is dependent on the nominal wavelength of the laser used for the measurement. For the measurement cases considered in this work, frequency-doubled Nd:YVO_4 diode-pumped solid-state lasers are utilized, so molecular iodine is the vapor of choice due to its sharp absorption features in the vicinity of 532 nm light (Miles et al. (1991)). This enables the attenuation of Mie and geometric scattering, while allowing a fraction of the LRS signal to pass through.

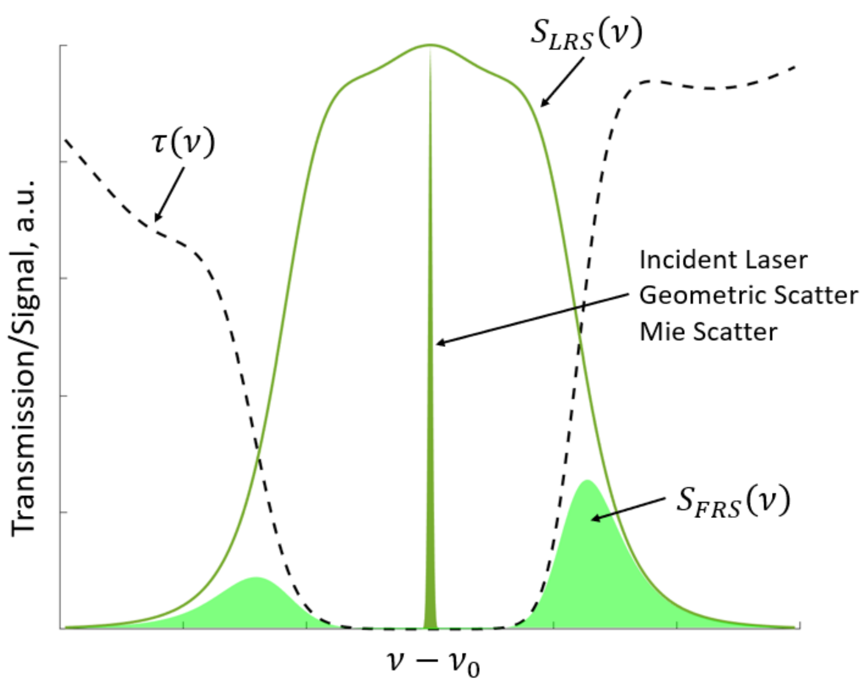

Figure 1. Spectral filtering diagram for FRS. After being filtered by the vapor cell, the detected signal is the area of the resulting $S_{FRS}(\nu)$ curve.

Different FRS techniques exist, but the one under consideration for this work is the frequency-scanning method (FSM) (Miles et al. (1996)). The FSM-FRS method works by tuning the laser to several, carefully chosen optical frequencies in the vicinity of a sufficiently sharp transmission feature of the vapor filter. If one acquires an image at each frequency, the resulting data is a spectrum at each pixel (or bin of pixels) in the image set. As discussed by Doll et al. (2014) and Boyda et al. (2020), if the measurement practitioner chooses a frequency scan range such that the vapor filter transmission is less that 10^{-5}, one can fully attenuate contributions from Mie and geometric scattering, while maximizing the detected spectral content of the desired LRS signal. This methodology, however, sacrifices the time resolution of desired flow properties, since the flow field will be time-averaged over the full acquisition time necessary to tune the laser and acquire an image at each frequency. Note: from here on, any discussion of FRS data is referring to the FSM-FRS method.

1.1. FRS Measurement Model

The following analysis will consider a single, general form for the FRS measurement model in order to appropriately evaluate the data under consideration. Following a similar nomenclature as Boyda et al. (2020) and Doll et al. (2016), the FRS measurement model for aerodynamic measurements is as follows:

$$S_{FRS}(\nu_0) = R\sigma_\Omega(\phi)\rho\left(\int_{-\infty}^{\infty} S_{LRS}(X,Y)\mathcal{T}(\nu-\nu_0+\Delta\nu_D)d\nu + B\left(\nu_0,\Delta\nu_D,IR_{Mie},IR_{Bknd}\right)\right) \tag{1}$$

with

$$\begin{aligned} B\left(\nu_0,\Delta\nu_D,IR_{Mie},IR_{Bknd}\right) = IR_{Mie}&\int_{-\infty}^{\infty} S_{Mie}(\nu-\nu_0)\mathcal{T}(\nu-\nu_0+\Delta\nu_D)d\nu + \\ IR_{Bknd}&\int_{-\infty}^{\infty} S_{Bknd}(\nu-\nu_0)\mathcal{T}(\nu-\nu_0)d\nu + C(\nu_0) \end{aligned} \tag{2}$$

$$Y = \frac{p}{\sqrt{2}Ku_0\eta} = \frac{\rho R_{air}T}{\sqrt{2}Ku_0\eta} \tag{3}$$

$$X = \frac{2\pi(\nu-\nu_0)}{\sqrt{2}Ku_0} \tag{4}$$

where, X is a non-dimensional frequency, and Y is a non-dimensional thermodynamic parameter that is defined as the ratio of the scattering wavelength to the mean free path between molecules (Miles et al. (2001)). ν_0 is the central frequency of the incident laser light, $\Delta\nu_D$ is the Doppler frequency shift due to bulk flow velocity, T is static temperature, p is static pressure, and ρ is static density. K is the magnitude of the scattering wave vector and is defined as $K = 4\pi\nu_0\sin\left(\theta/2\right)/c$. θ is the scattering angle (i.e., angle between laser propagation direction, $\hat{i}$, and observation direction,

$\hat{o}$). $u_0 = \sqrt{k_B T/m}$ is the most probable molecular velocity, and η is the shear (or dynamic) viscosity of the scattering medium. X and Y are commonly used terms to describe the Rayleigh-Brillouin scattering (RBS) lineshape, which can be modeled by Tenti et al. (1974)'s model (generally defined as the Tenti S6 model). While the Tenti S6 was derived for molecular gases, and not mixtures, it has been shown to agree with measured RBS in air for Y between 0.4 and 1.7 at $\theta = 90^\circ$ (Gu & Ubachs (2014)).

$\sigma_\Omega(\phi)$ is the polarization-dependent differential Rayleigh scattering cross-section with ϕ being the angle between polarization direction of the incident electric field and the observation direction. A depiction of Rayleigh scattering intensity angular dependence is shown in Fig. 2 below. This figure provides insights into how the detected intensity of Rayleigh-scattered light changes for linearly polarized light. For example, maximum Rayleigh scattering intensity would occur when the observation direction is perpendicular to the polarization direction ($\phi = 90^\circ$).

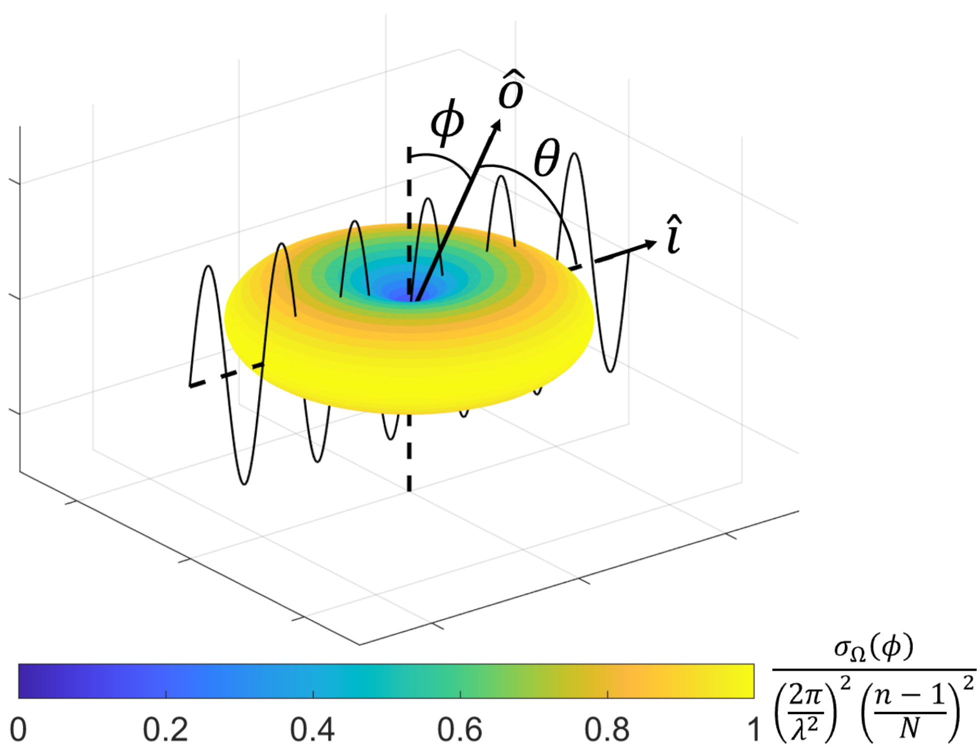

Figure 2. $\sin^2(\phi)$ directivity for Rayleigh scattering intensity from a linearly polarized incident electric field.

What distinguishes the measurement from the pure FRS signal is a gain parameter, R, which is a measurement setup-specific constant (e.g., contains information about local collection efficiency, incident laser power, detector exposure time, etc.), and a signal bias parameter, B, which contains information about all other possible contributions to the detected FRS signal (e.g., Mie scatter, geometric/background scatter). In certain, applied measurement cases, it may be of interest to quantify intensity contributions from Mie scattering and/or background scattering. In these cases, an intensity ratio (IR) term may be incorporated into the signal model equation as shown in Eq. (2) (Boyda et al. (2020)). In most scenarios, these terms may be neglected if one performs a frequency scan such that the vapor filter transmission is less than 10^{-5} (as mentioned earlier). The additional parameter in Eq. (2), $C(\nu_0)$, is comprised of all additional contributions to the measured FRS signal that may or may not be modelable. As will be discussed in Section 3.2, $C(\nu_0)$ could also contain frequency-dependent signal contributions due to modeling error. In a controlled laboratory environment, one could perform a series of calibration measurements, such as evacuating the test section or introducing a reference gas with well-defined differential scattering cross-section before or after running the measurement of interest to quantify $C(\nu_0)$ (Cutler & Lowe (2023)). However, this procedure may be impractical for applied measurements (as is the case for experiments considered in this work).

The aim of this paper is to utilize an FRS database that covers a broad range of possible measurement configurations and flow cases to understand what the source(s) of bias are for these applied measurements. A qualitative approach will be introduced in the form of Quantile-Quantile (Q-Q) analysis to, generally, assess when modeled signals agree with measured signals, and when they do not. Following this, biases of key quantities to FRS multi-property quantification will be determined to see if there is a particular range of measurement configurations where biases are minimal. Perhaps more importantly, this quantitative bias analysis will provide insights into what configurations have larger biases.

The remainder of this paper will proceed as follows. Section 2 will overview the extensive FRS database to be analyzed in this work, along with the Q-Q analysis method used to compare measured to modeled signals. Section 3.1 will present some results of this qualitative analysis, and discuss the immediate path forward of analyzing the signal bias-induced flow property bias. Section 3.2 will overview the non-dimensional flow property bias results along with implications for unbiased measurement configurations. Finally, Section 4 will provide a summary of the present work.

2. Methodology

2.1. Description of FRS Data

Table 1 describes several different FRS experiments that will be the focus of this work. Each experiment (labeled Test 1 - 6) has a specified Y range, nominal signal-to-noise ratio (SNR), high-level setup configuration (light delivery and collection), and whether or not each measurement has an associated reference/validation measurement for the flow field of interest. The scattering medium is air for all test cases. SNR, for this work, is defined as: $\mathrm{SNR}(dB) = 10\log_{10}[\sigma_S^2/(\sigma_P^2+\sigma_G^2)]$, where σ_S^2 is the variance of the noise-free FRS signal, σ_P^2 is the variance of the Poisson-distributed shot noise contribution to the total FRS signal, and σ_G^2 is the variance of the Gaussian-distributed random noise contribution to the total FRS signal. σ_S^2 is determined by computing the mean-square (along the optical frequency dimension) of the model signal fit to the measured signals, which would be an approximation to the noise-free signal. The procedure for this model curve fitting will be discussed in Section 3.2. $\sigma_P^2+\sigma_G^2$ is estimated by computing the sample variance of the difference of the measured FRS signal and the fitted model signal.

For the high-level description of light delivery, "Free Space" indicates that the laser light was delivered to the measurement volume via free-space optics (e.g., mirrors, lenses, etc.). "Fiber" indicates that the laser light was delivered via a multimode fiber optic patch cable. For the high-level description of light collection, "Direct" indicates that the scattered light was directly imaged by a camera equipped with a single imaging lens. "Fiber Bundle" indicates that the scattered light was first collected by an imaging fiber bundle, where the image was then propagated through the bundle and projected onto a camera sensor via two lenses in relay configuration.

Table 1. FRS database table to be used for data mining and analysis.

Test ID	Flow Off Y	Flow On Y	SNR (dB)	Light Delivery	Light Collection	Reference Data?
Test 1	1.19 – 1.64	0.74 – 1.53	16	Free Space	Direct	Yes
Test 2	1.36 – 2.05	--	18	Free Space	Direct	No
Test 3	1.28 – 1.72	1.14 – 1.50	12	Free Space	Direct	Yes
Test 4	0.68 – 0.94	--	12	Free Space	Direct	No
Test 5	0.57 – 0.58	0.54 – 0.58	30	Free Space	Direct	Yes
Test 6	0.62 – 2.05	0.53 – 1.71	20	Fiber	Fiber Bundle	Yes

For each measurement case, θ is determined by computing the angle between the observation direction vector, $\hat{o}$, and the laser propagation direction vector, $\hat{\imath}$. The distribution of $\hat{o}$ across the measurement field for each imaging perspective is computed based on a standard camera calibration procedure that derives a pinhole camera model that is used to (1) determine camera locations in world coordinates (i.e., mm) and (2) obtain a direct mapping from pixel coordinates to world coordinates (Tsai (1987)). The distribution of $\hat{\imath}$ across the field is determined either by practitioner knowledge of laser propagation direction in the world frame or through a laser calibration procedure that computes direction vectors based on the distribution of the laser line/sheet across a camera calibration image. The uncertainty in the computed θ was calculated to be within $0.5°$ for the above procedure and, therefore, is considered not to contribute to any potential disagreement between measured and modeled signals.

2.2. Qualitative Analysis Methodology

This work utilizes a Q-Q plot analysis to assess when FRS measurement data is agreeable to traditional FRS signal models, and when it is not. Generally, Q-Q plots are utilized as a statistical visualization tool to compare two distributions and can reveal outlier information and/or trends in one distribution relative to the other (Marden (2004)). If one distribution agrees with the other, then the sample points will collapse along a line with slope of one and intercept of zero (i.e., $y = x$). As discussed in Section 1, the difference between acquired FRS signals and modelable signals is in a scale factor, R, and a signal bias parameter, B (Eq. (1)). To get measured and modeled signals on the same relative scale, both signals are normalized by their mean value. Additionally, to remove sensitivity to the Mie and background scattering portions of B, signals are only evaluated in frequency such that the model vapor filter transmission is less than 10^{-5}. This procedure enables a direct comparison between measured and modeled signals such that the only parameter in Eq. (1) that could cause disagreement is $C(\nu_0)$. The mean-normalized measurement model is shown in Eq. (5) below.

$$\frac{S_{FRS}(\nu_0)}{\mu_{S_{FRS}}} = \frac{\int_{-\infty}^{\infty} S_{LRS}(X,Y)\mathcal{T}(\nu-\nu_0+\Delta\nu_D)d\nu + C(\nu_0)}{\frac{1}{L}\sum_{j=1}^{L}\left[\int_{-\infty}^{\infty} S_{LRS}(X,Y)\mathcal{T}(\nu-\nu_0+\Delta\nu_D)d\nu + C(\nu_0)\right]_j} \quad \text{for} \;\; \mathcal{T}(\nu-\nu_0+\Delta\nu_D) < 10^{-5} \tag{5}$$

where, L is the number of discrete signal points over the range of ν_0 where $\mathcal{T} < 10^{-5}$.

If one scales measured FRS signals in this manner, the resulting signal will have the same functional form as the RHS of Eq. (5), which can easily be modeled since the only signal contributions are from S_{LRS} and $\mathcal{T}$. For this work, S_{LRS} is modeled with a MATLAB implementation of the Tenti S6 model for spontaneous RBS (SRBS). $\mathcal{T}$ is modeled using calibrated vapor filter transmission models that have been calibrated over the frequency tuning range of the laser used for the FRS measurements considered in this work. From this point, mean-normalized measured FRS signals will be denoted as $\hat{S}_{Meas}$ (LHS of Eq. (5)), and mean-normalized modeled FRS signals will be denoted as $\hat{S}_{Mod}$ (RHS of Eq. (5)).

3. Results & Discussion

3.1. Q-Q Plot Analysis

The following results will display Q-Q plots of $\hat{S}_{Mod}$ vs. $\hat{S}_{Meas}$ at flow-off (ambient thermodynamic conditions and zero flow velocity) and flow-on conditions for several Y across the measurement volumes. Figure 3 displays the results of this measured-to-modeled signal comparison study for all measurement configurations at the flow-off condition. From observing this figure, there is a clear relationship between measured-to-modeled signal agreement and Y. The relationship is that as Y decreases, the agreement between modeled and measured signals improves. The observed behavior is consistent amongst all test configurations, but is more obvious when observing Fig. 3(F) due to the larger range of Y for Test 6.

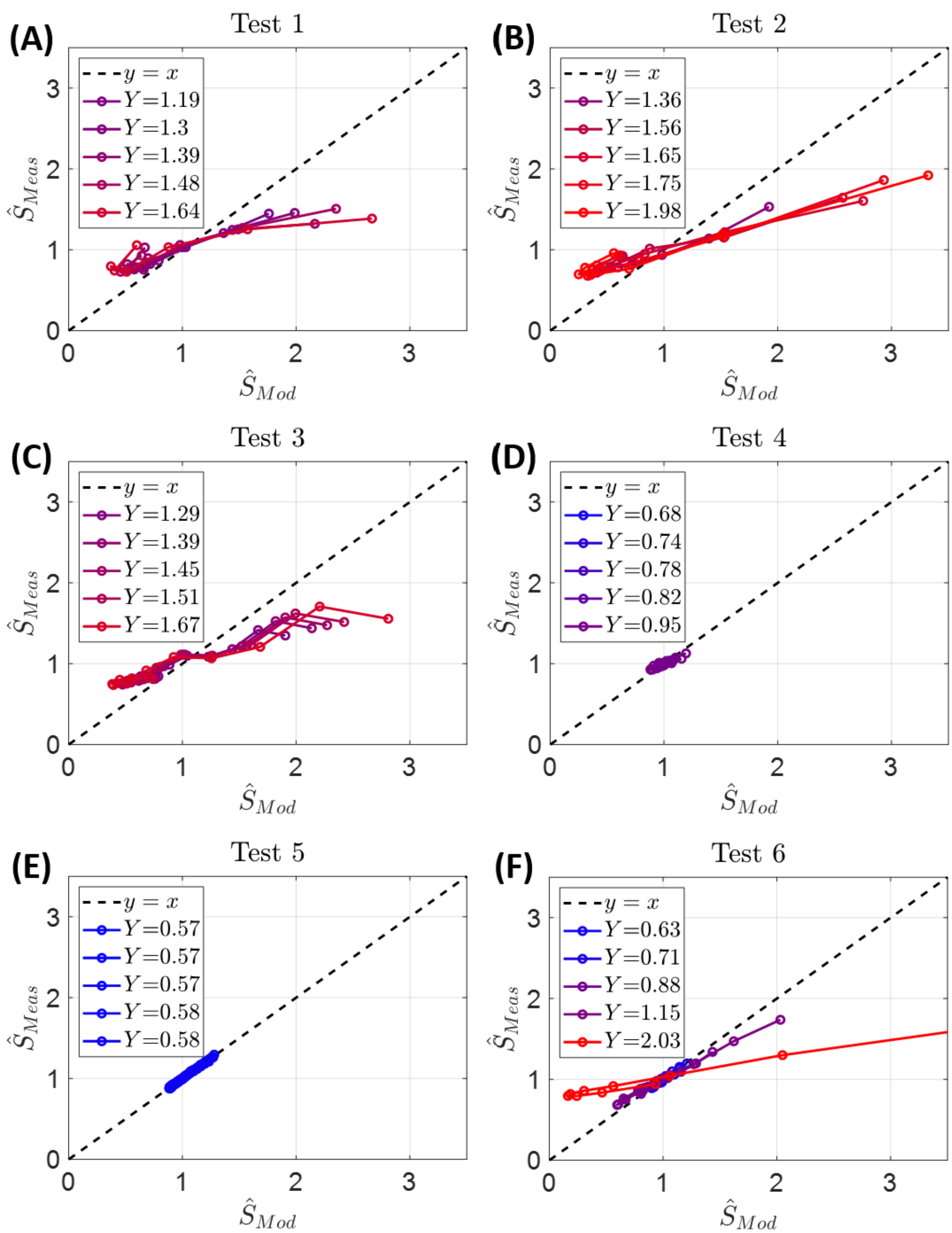

Figure 3. Q-Q plots for all test configurations at flow-off condition.

In a similar manner as Fig. 3, Fig. 4 displays the Q-Q plots at the flow-on condition. The local flow field quantities were determined by reference probe measurements that were then used as inputs when generating modeled signals. As indicated by Table 1, only four of the test configurations had reference measurements associated with them. Observing this figure indicates that, once again, measured-to-modeled signal agreement improves as Y decreases. Since the same behavior is shown between flow-off and flow-on conditions, and across each of these different test configurations, a generalization can be made that the signal disagreement is from the same source that yields a Y dependence on $C(\nu_0)$ from Eq. (1). The authors acknowledge that, in practice, one could solve for local values of $C(\nu_0)$ using the flow-off FRS signals and apply those values to flow-on data during post processing. The remainder of this current work will focus on solving for flow properties from FRS data using nonlinear least-squares approaches. This will be done for both flow-off and flow-on conditions to quantitatively assess how the behavior of $C(\nu_0)$ influences flow property bias uncertainty

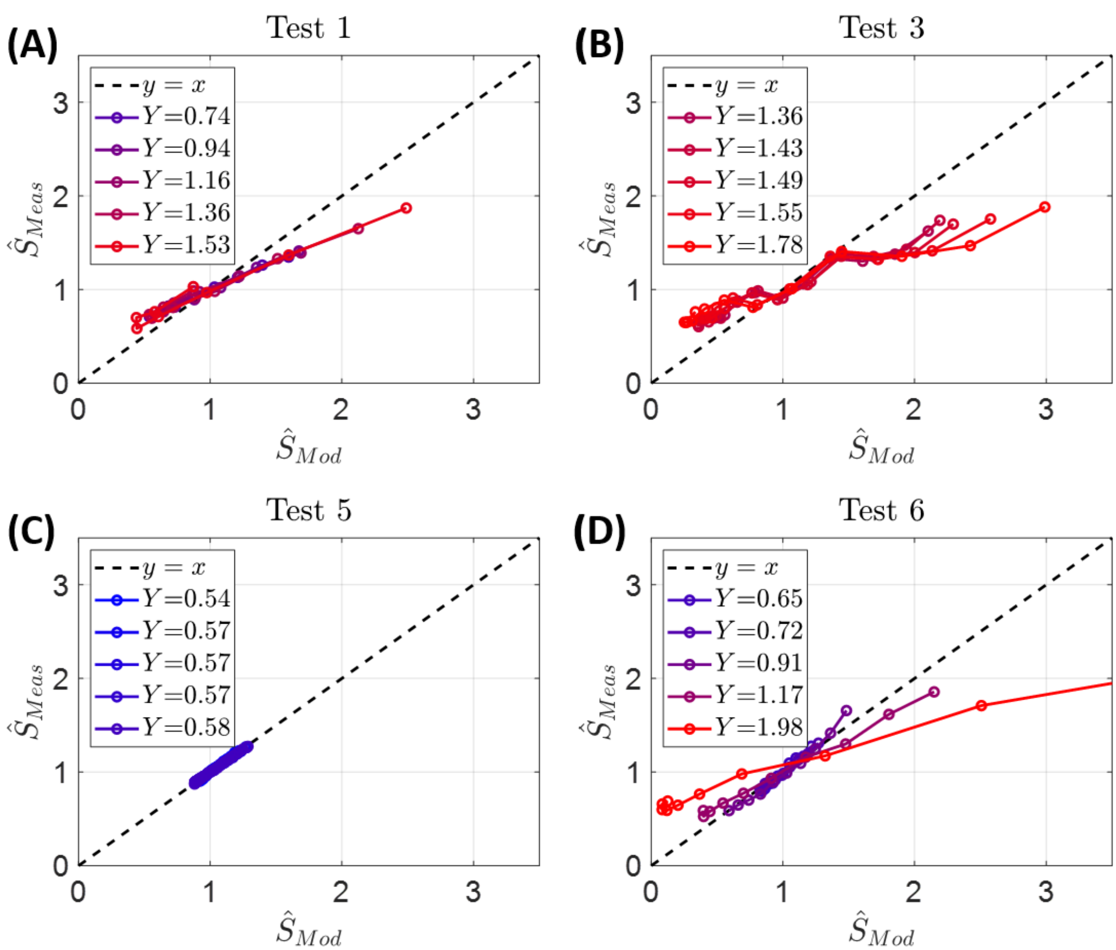

Figure 4. Q-Q plots for all test configurations at flow-on condition.

3.2. Flow Property Bias Uncertainty Analysis

For each measurement configuration, local values for $R\sigma_\Omega\rho$ (note: while these are typically three separate parameters, they are considered here as a single scalar parameter), Y, and ΔX_D, were determined via nonlinear least-squares (NLLS) (Moré (2006)). The stopping criterion for the NLLS algorithm was such that convergence would be reached if the objective function changed less than 10^{-15}, the solution parameters changed less than 10^{-15}, or if 400 solver iterations was achieved. Y was computed instead of thermodynamic quantities, and ΔX_D instead of Doppler frequency shift in order to make the results universally interpretable. Local field quantities were known for the flow-off condition due to knowledge of ambient values, and for the flow-on condition due to reference probe measurements (i.e., with attendant uncertainties). Since the reference measurements provided thermodynamic quantities and velocities, they needed to be converted to Y and ΔX_D for direct comparison to the FRS results. Propagating reference measurement uncertainties through Eq. (4) and Eq. (3) yielded 95% confidence uncertainties of 5×10^{-3} and 5×10^{-6} for Y and ΔX_D, respectively.

Due to non-negligible signal bias trends from $C(\nu_0)$ (discussed above), the NLLS solution for Y was biased with respect to known quantities. Note: biases in Y will only be discussed from here on, since it was observed that Y was much more sensitive to signal model disagreement than ΔX_D. To show this, histograms of the residuals between the NLLS solution for Y (denoted Y_{opt}) and the reference values for Y (denoted Y_{ref}) are shown in Fig. 5.

The data shown in these histograms are from all of the measurements (Tests 1-6) and both the flow-off and flow-on cases. This is to demonstrate that there are, in general, two modes for the distribution of Y residuals across all of these very different measurements and flow cases. One of these modes, which will be denoted as the "least-biased mode," is shown as the blue histogram in Fig. 5 and corresponds to conditions where $Y_{ref} \leq 1$. The other mode, which will be denoted as the "biased mode," is shown as the orange histogram in Fig. 5 and corresponds to conditions where $Y_{ref} > 1$. From this plot, one can make two generalizations. The first generalization is that $C(\nu_0)$ is less influential (or is negligible) for measurement configurations where $Y \leq 1$. Consequently, the second generalization is that least-biased measurement configurations seem to occur when $Y \leq 1$.

To further understand the significance of these results, the general contributions to $C(\nu_0)$ will be summarized and discussed in the context of this work to conclude what the root cause appears to be for this modeled-to-measurement signal disagreement. These contributions are as follows:

1. Signal noise sources (e.g., Poisson-distributed photon shot noise, Gaussian-distributed sensor read noise).
2. Constant offset from the detector (i.e., "dark" signal).
3. Stray light (or other scattering sources) along optical path to detector unit that is not filtered

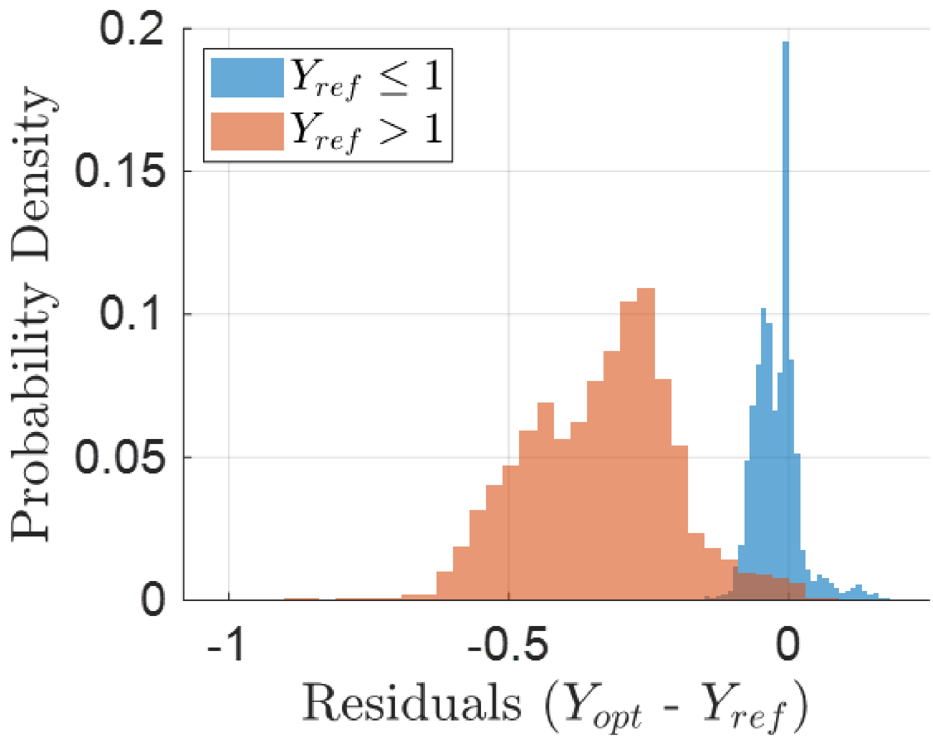

Figure 5. Histogram of Y residuals across all measurements considered in this work. Each mode of this bimodal distribution is separated into residuals where $Y_{ref} \leq 1$ (blue) and $Y_{ref} > 1$ (orange).

by the vapor cell or laser line filter.

4. Model uncertainty for vapor filter transmission.
5. Spectral broadening of incident laser light prior to measurement volume interrogation.
6. Model uncertainty in the RBS spectrum.
7. Uncertainty in frequency values (absolute or relative) for FSM-FRS method.

For item 1, this contribution can be reduced by averaging FRS signals from repeated datasets of the same flow field/measurement configuration. However, if repeated sets are not practically feasible due to facility constraints, for example, then low sensor noise detection hardware should be utilized. In either situation, signal noise should only contribute to the random variation of flow field results and not to any bias trends. Therefore, this item was not considered to contribute to the trend in biases shown above. For items 2 and 3, these contributions can be mitigated by subtracting a "dark image" from all measured images and are acquired by blocking the laser light from entering the measurement volume. Items 4-7 are the contributions that remain relevant to the current work. Item 4 can be mitigated by performing precise measurements of the vapor cell hardware used for FRS measurements to get a calibrated transmission model (e.g., utilizing a similar procedure as

Forkey et al. (1997)). As discussed earlier, the iodine transmission model used in this work was one that was calibrated over the achievable frequency scan range of the laser used for these measurements. Since calibrated models were used, item 4 is considered to be a negligible contribution to flow property biases. Item 5 is a contribution that is specific to FRS applications in the vicinity of harsh environments, where several interfering inputs may cause broadening of the incident laser prior to interrogating the measurement volume. This broadening would go against a fundamental assumption generally made for FRS measurements that the incident laser interrogating the measurement volume is (sufficiently) narrow band. Considering that the most fundamental form of the FRS measurement model from Forkey (1996) contains contributions from the incident laser spectrum, it is understood that a broadened laser line has a significant impact on the behavior of FRS signals, and, therefore, the resulting flow properties. The contribution for item 7 is due to uncertainty arising from the laser frequency monitoring system used for an FSM-FRS measurement. The influence of this uncertainty can be reduced by utilizing a high-precision wavelength meter, or an iodine transmission-based scheme that maps the transmission of a reference vapor cell to laser frequency via comparison to Forkey et al. (1997)'s model. In the measurement cases considered in this work, the latter approach was used to quantify laser frequency at each scan point.

Each of the measurement configurations that were analyzed in this work had different setups in terms of camera hardware and positions, laser light source and delivery hardware, vapor cell hardware, and flow condition. The trends in biases from this work, however, indicate that there is some common source that induces such biases. Since these configurations were so different from a hardware and flow condition standpoint, it is unlikely that incident laser broadening was the common source of bias. Additionally, the laser frequency monitoring system did not indicate any appreciable broadening of the incident laser line. The only similarity between each of these measurement configurations is how the measured FRS signals were evaluated. In other words, the modeled signals that were used to evaluate measured signals. The only signals that were modeled in this work were the RBS signal and the iodine transmission signal. As discussed earlier, the iodine transmission models were calibrated for each vapor cell hardware. Therefore, this points to the RBS model for air as the main source of these biases.

To give some insights into what certain behaviors of the modeled RBS lineshape could be inducing bias, Fig. 6 below shows some example lineshapes for the case where $Y \leq 1$ (blue) and where $Y > 1$ (orange). From this plot, one can observe that for $Y > 1$, the Stokes/anti-Stokes Brillouin scattering contributions become more pronounced (these are the two symmetric peaks that are offset from zero relative wavenumber on the orange curve). These contributions are not as pronounced for $Y \leq 1$, which is the "least-biased" regime as shown in Fig. 5. This observation may provide some insights into the physical mechanism that is causing the biases discussed in this work. While an in-depth investigation of this is still necessary, an empirical correction to the RBS model is required for $Y > 1$.

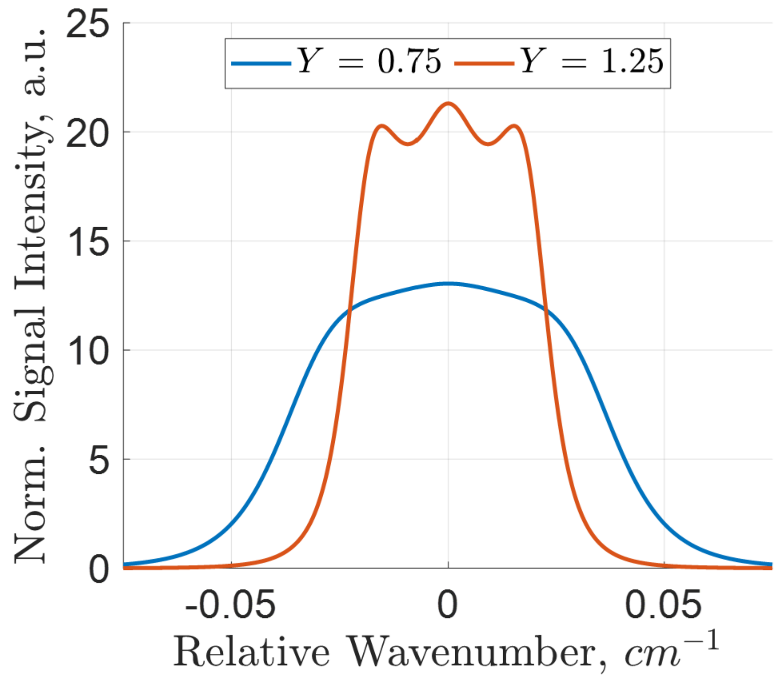

Figure 6. Representative RBS lineshapes for air from the Tenti S6 model for the case where $Y \leq 1$ (blue curve) and $Y > 1$ (orange curve).

4. Conclusions

This work has shown a data-driven analysis in the form of Q-Q plots to assess how well measured FRS signals for different measurement configurations agree with traditional signal models. The general conclusion of this qualitative analysis was that measured signals tend to agree more closely to modeled signals at lower values of Y. Additionally, the non-negligible behavior of the signal bias parameter, $C(\nu_0)$, was discussed to be the main contributing factor to disagreements between modeled and measured signals.

To understand how $C(\nu_0)$ influences results obtained from FRS data, non-dimensional parameters of Y and ΔX_D were quantified via NLLS. Reference measurements of the flow field of interest for each experiment were used to obtain known values for Y. The residuals between the NLLS solution for Y (Y_{opt}) and the reference values (Y_{ref}) where plotted on a histogram to assess any noticeable trends in the probability distribution. The resulting bimodal distribution was separated into a "least-biased mode" and a "biased mode," which corresponds to $Y_{ref} \leq 1$ and $Y_{ref} > 1$, respectively. This separation of modes led to the conclusion that the behavior of $C(\nu_0)$ is less influential (or can be neglected) for measurement configurations where $Y_{ref} \leq 1$.

An assessment of the relevant contributions to $C(\nu_0)$ in the context of the measurements analyzed for this work indicates that the modeling of the RBS signal for air is the most probable source of bias uncertainty. Observation of representative RBS lineshapes from the Tenti S6 model shows that the Brillouin scattering contributions are more prominent for $Y > 1$, which may indicate that this portion of the signal is not modeled correctly. To drive down bias uncertainty associated with multi-property FRS measurements in air, especially for cases where $Y > 1$, an empirical correction to the model used to evaluate FRS signals is required.

Nomenclature

FRS	filtered Rayleigh scattering
LRS	laser Rayleigh scattering
NLLS	nonlinear least-squares
Nd:YVO_4	Neodymium-doped yttrium orthovanadate
FSM	frequency scanning method
Q-Q	Quantile-Quantile
SNR	signal-to-noise ratio
RBS	Rayleigh-Brillouin scattering
SRBS	spontaneous Rayleigh-Brillouin scattering
LHS	left-hand side
RHS	right-hand side
S_{FRS}	FRS signal
S_{LRS}	LRS signal
$\mathcal{T}$	iodine vapor filter transmission
ν_0	central frequency/wavenumber of incident laser
$\Delta\nu_D$	Doppler frequency shift
K	magnitude of the scattering wave vector
c	speed of light
u_0	most probable molecular speed
k_B	Boltzmann constant
m	molecular mass of the fluid
η	shear/dynamic viscosity
R_{air}	specific gas constant for air
Y	ratio of scattering wavelength to the mean free path
X	non-dimensional frequency
T	static temperature
N	molecular number density
n	refractive index of the scattering medium
ρ	static density
θ	scattering angle
$\hat{o}$	unit vector in observation direction

$\hat{i}$	unit vector in laser propagation direction
ϕ	observation angle with respect to the polarization direction
σ_Ω	differential Rayleigh scattering cross-section
R	measurement setup-specific constant
B	signal bias parameter
C	all additional contributions to FRS signal
IR_{Mie}	Mie scattering intensity ratio
IR_{Bknd}	background/geometric scattering intensity ratio
S_{Mie}	Mie scattering spectrum
S_{Bknd}	background/geometric scattering spectrum
p	static pressure
λ	laser wavelength
$\mu_{S_{FRS}}$	mean value of FRS signal
ΔX_D	non-dimensional Doppler frequency shift
σ_S^2	variance of the noise-free FRS signal
σ_P^2	variance of the shot noise contribution to FRS signal
σ_G^2	variance of the random noise contribution to FRS signal
$\hat{S}_{Mod}$	mean-normalized modeled FRS signal
$\hat{S}_{Meas}$	mean-normalized measured FRS signal

References

Boguszko, M., & Elliott, G. (2005). Property measurement utilizing atomic/molecular filter-based diagnostics. *Progress in Aerospace Sciences*, *41*(2), 93–142.

Boyda, M. T., Byun, G., Saltzman, A. J., & Lowe, T. (2020). Influence of mie and geometric scattering contributions on temperature and density measurements in filtered rayleigh scattering. In *Aiaa scitech 2020 forum* (p. 1516).

Cutler, A. D., & Lowe, K. T. (2023). Laser rayleigh scattering, filtered rayleigh scattering, and interferometric rayleigh scattering. In *Optical diagnostics for reacting and non-reacting flows: Theory and practice* (p. 75-136). Retrieved from `https://arc.aiaa.org/doi/abs/10.2514/5.9781624106330.0075.0136` doi: 10.2514/5.9781624106330.0075.0136

Doll, U., Burow, E., Stockhausen, G., & Willert, C. (2016). Methods to improve pressure, temperature and velocity accuracies of filtered rayleigh scattering measurements in gaseous flows. *Measurement Science and Technology*, *27*(12), 125204.

Doll, U., Stockhausen, G., & Willert, C. (2014). Endoscopic filtered rayleigh scattering for the analysis of ducted gas flows. *Experiments in Fluids*, *55*(3), 1–13.

Forkey, J. N. (1996). *Development and demonstration of filtered rayleigh scattering: a laser based flow diagnostic for planar measurement of velocity, temperature and pressure*. PhD Dissertation, Princeton University.

Forkey, J. N., Lempert, W. R., & Miles, R. B. (1997). Corrected and calibrated i2 absorption model at frequency-doubled nd:yag laser wavelengths. *Applied optics*, *36*(27), 6729–6738.

Gu, Z., & Ubachs, W. (2014). A systematic study of rayleigh-brillouin scattering in air, n2, and o2 gases. *The Journal of chemical physics*, *141*(10).

Marden, J. I. (2004). Positions and qq plots. *Statistical Science*, 606–614.

Miles, R., Forkey, J., Finkelstein, N., & Lempert, W. (1996). Precision whole-field velocity measurements with frequency-scanned filtered rayleigh scattering. In *Developments in laser techniques and applications to fluid mechanics* (pp. 463–477). Springer.

Miles, R., Lempert, W., & Forkey, J. (1991). Instantaneous velocity fields and background suppression by filtered rayleigh scattering. In *29th aerospace sciences meeting* (p. 357).

Miles, R., Lempert, W., & Forkey, J. (2001). Laser rayleigh scattering. *Measurement Science and Technology*, *12*(5), R33.

Moré, J. J. (2006). The levenberg-marquardt algorithm: implementation and theory. In *Numerical analysis: proceedings of the biennial conference held at dundee, june 28–july 1, 1977* (pp. 105–116).

Tenti, G., Boley, C., & Desai, R. C. (1974). On the kinetic model description of rayleigh–brillouin scattering from molecular gases. *Canadian Journal of Physics*, *52*(4), 285–290.

Tsai, R. (1987). A versatile camera calibration technique for high-accuracy 3d machine vision metrology using off-the-shelf tv cameras and lenses. *IEEE Journal on Robotics and Automation*, *3*(4), 323–344.